



# The 2016 $M_{\rm w}$ 7.8 Pedernales, Ecuador, Earthquake: Rapid Response Deployment

by Anne Meltzer, Susan Beck, Mario Ruiz, Mariah Hoskins, Lillian Soto-Cordero, Joshua C. Stachnik, Colton Lynner, Rob Porritt, Daniel Portner, Alexandra Alvarado, Stephen Hernandez, Hugo Yepes, Philippe Charvis, Yvonne Font, Marc Regnier, Hans Agurto-Detzel, Andreas Rietbrock, Sergio Leon-Rios, and E. Diego Mercerat

#### **ABSTRACT**

The April 2016 Pedernales earthquake ruptured a 100 km by 40 km segment of the subduction zone along the coast of Ecuador in an  $M_{\rm w}$  7.8 megathrust event east of the intersection of the Carnegie ridge with the trench. This portion of the subduction zone has ruptured on decadal time scales in similar size and larger earthquakes, and exhibits a range of slip behaviors, variations in segmentation, and degree of plate coupling along strike. Immediately after the earthquake, an international rapid response effort coordinated by the Instituto Geofísico at the Escuela Politécnica Nacional in Quito deployed 55 seismometers and 10 ocean-bottom seismometers above the rupture zone and adjacent areas to record aftershocks. In this article, we describe the details of the U.S. portion of the rapid response and present an earthquake catalog from May 2016 to May 2017 produced using data recorded by these stations. Aftershocks focus in distinct clusters within and around the rupture area and match spatial patterns observed in long-term seismicity. For the first two and a half months, aftershocks exhibit a relatively sharp cutoff to the north of the mainshock rupture. In early July, an earthquake swarm occurred ~100 km to the northeast of the mainshock in the epicentral region of an  $M_{\rm w}$  7.8 earthquake in 1958. In December, an increase in seismicity occurred  $\sim$ 70 km to the northeast of the mainshock in the epicentral region of the 1906 earthquake. Data from the Pedernales earthquake and aftershock sequence recorded by permanent seismic and geodetic networks in Ecuador and the dense aftershock deployment provide an opportunity to examine the persistence of asperities for large to great earthquakes over multiple seismic cycles, the role of asperities and slow slip in subduction-zone megathrust rupture, and the relationship

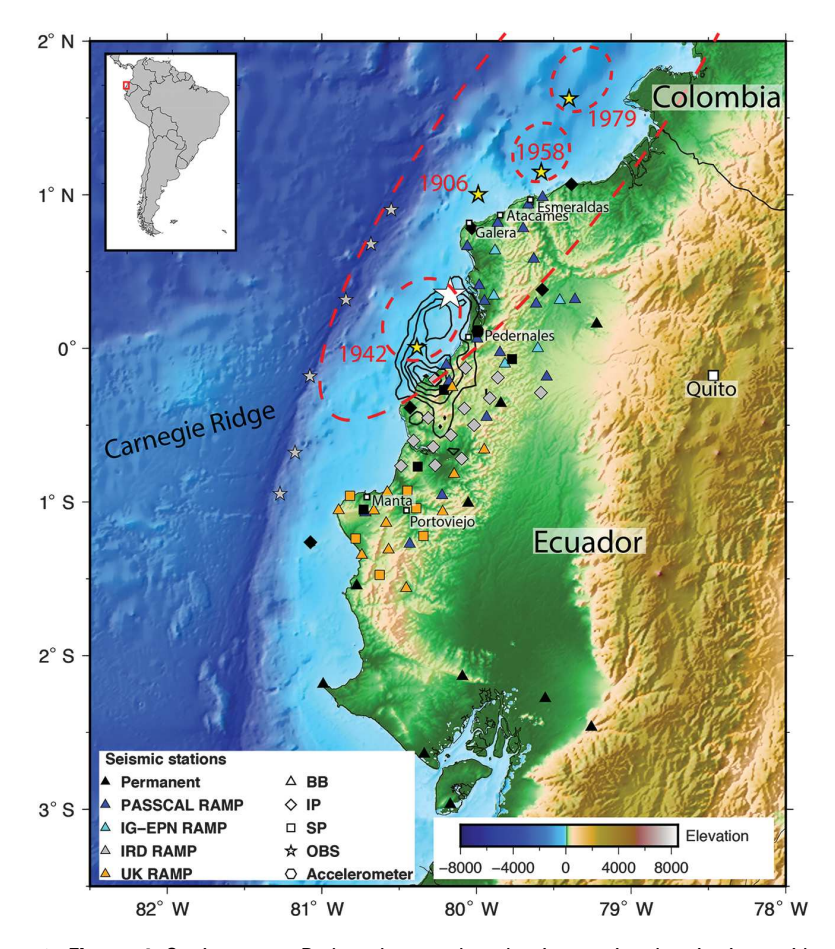
between locked and creeping parts of the subduction interface.

Supplemental Content: Figures showing station uptime for the Incorporated Research Institutions for Seismology-Portable Array Seismic Studies of the Continental Lithosphere (IRIS-PASSCAL) Ecuador Rapid Array Mobilization Procedure (RAMP) deployment, station map, and stations sites in Google Earth, representative frequency-dependent noise levels for coastal EC16, bedrock EC19, and EC15 inland stations using the power spectral density probability density function noise toolkit provided by the IRIS Data Management Center (DMC), maps of postseismic events in the automatic catalog produced from IRIS-PASSCAL stations, errors and magnitude of completeness and b-value, animation of Pedernales earthquake postseismic sequence from the automatic catalog produced from IRIS-PASSCAL stations, and table of station name, location (latitude, longitude, and elevation), sensor type, installation date, demobilization date, percent uptime, site characteristics, and comments. Also showing the details of station design, sensor vault, station box, and station photos, and a digital file of the earthquake catalog in QuakeML format.

## INTRODUCTION

Subduction-zone megathrust faults generate the largest earth-quakes and devastating tsunami. A spectrum of slip behaviors including earthquakes, nonvolcanic tremor, slow-slip events (SSEs), low-frequency earthquakes (LFEs) and very LFEs is observed in many subduction zones contributing to the seismic cycle that ultimately culminates in large subduction-zone earthquakes (Dragert et al., 2001; Lowry et al., 2001; Obara, 2002; Rogers and Dragert, 2003; Schwartz and Rokosky, 2007; Shelly et al., 2007; Brown et al., 2009, 2013; Peterson and Christensen, 2009; Peng and Gomberg, 2010; Ide, 2012; Wallace and Eberhart-Phillips, 2013; Saffer and Wallace, 2015; Bilek and Lay, 2018). Lateral variations in structure or mechanical properties in the subduction zone, roughness on the downgoing plate, seamounts, seafloor offsets,

1346 Seismological Research Letters Volume 90, Number 3 May/June 2019



▲ Figure 1. Station map Pedernales earthquake international seismic rapid response. (Inset) South America, Ecuador outlined by red box. 2016 Pedernales earthquake mainshock location (white star) and coseismic slip contours from Nocquet et al. (2017), coseismic slip contour 1 m, and maximum slip 6 m. Coastal stations from the permanent national network in black, other colors in key designate temporary stations. BB, broadband sensors; IG-EPN, Instituto Geofísico at the Escuela Politécnica Nacional; IP, intermediate period sensors; OBS, ocean-bottom seismometer; PASSCAL, Portable Array Seismic Studies of the Continental Lithosphere; RAMP, Rapid Array Mobilization Procedure; SP, short-period sensors. Historic earthquakes, epicenters yellow stars, and estimated rupture areas red dashed ellipses after Swenson and Beck (1996), Beck and Ruff (1984), and Collot et al. (2004).

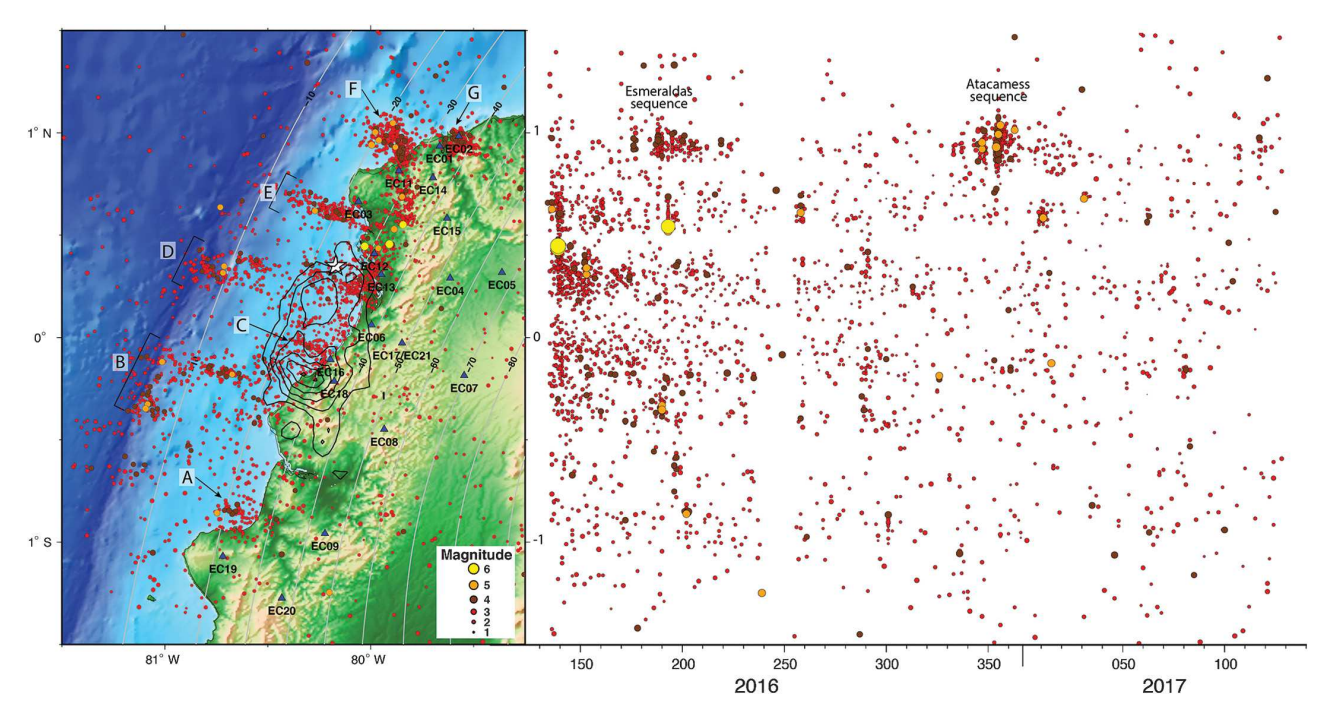
ridges, and sediments segment the subduction zone and can act as asperities or as barriers inhibiting rupture (Kodaira, 2000; Husen and Kissling, 2002; Bangs et al., 2006; Wang and Bilek, 2011, 2014). Features within the overriding plate, batholiths, fore-arc basins, and faults can also influence rupture behavior (Hicks et al., 2014), and there are regions in the downgoing slab as well as earthquakes in the overriding plate that may be triggered by megathrust events (Sherrod and Gomberg, 2014). Linking physical processes to the spectrum of deformation and understanding the interactions between the range of slip behaviors and their contributions to the seismic cycle can

lead to improved hazard assessment and mitigation strategies (Brodsky and Lay, 2014; Kanamori, 2014).

On 16 April 2016, the  $M_{
m w}$  7.8 Pedernales earthquake ruptured an ~100 km long by 40 km wide section of the subduction-zone offshore Ecuador (Fig. 1; U.S. Geological Survey National Earthquake Information Center [USGS NEIC], 2016; Ye et al., 2016; Nocquet et al., 2017). The epicentral region of the mainshock lies east of the intersection of the Carnegie ridge with the subduction zone along a section of the margin where the orientation of the trench shifts from ~N20°E to  $\sim$ N32° E. In 1906, an  $M_{
m w}$  8.8 earthquake ruptured a 500 km section of the subduction zone from the Carnegie ridge to Colombia (Kelleher, 1972; Kanamori and McNally, 1982; Mayorga and Sánchez, 2016; Fig. 1). Smaller patches of the segment that ruptured in 1906 slipped from south to north in a series of major earthquakes: 1942  $M_{\rm w}$  7.8, 1958  $M_{\rm w}$  7.7, and 1979  $M_{\rm w}$  8.2 (Kanamori and McNally, 1982; Mendoza and Dewey, 1984; Swenson and Beck, 1996). The 2016 Pedernales earthquake ruptured the same portion of the subduction zone that slipped in 1942 (Ye et al., 2016; Nocquet et al., 2017). The death toll from this earthquake reached over 650. Close to 30,000 people were reported injured. Over 85,000 people received humanitarian assistance in the recovery and reconstruction phase (International Federation of Red Cross and Red Crescent Societies, 2016). The coastal cities of Manta, Portoviejo, and Pedernales sustained significant damage (Lanning et al., 2016; Franco et al., 2017; Goretti et al., 2017; Palacios et al., 2018). Economic loss and the cost of recovery and reconstruction were estimated at \$3.3 billion U.S., ~3% of Ecuadorian Gross Domestic Product (National Planning and Development Secretariat, Ecuador).

The 2016 Pedernales earthquake was preceded by an  $M_{\rm w}$  4.8 foreshock by 11 min. The mainshock rupture propagated from north

to south parallel to the subduction interface (USGS NEIC, 2016; Ye *et al.*, 2016; Nocquet *et al.*, 2017). Coseismic slip ranged from 1 to 6 m and occurred in two distinct patches (Nocquet *et al.*, 2017) at depths between 15 and 30 km (Fig. 1). The rupture corresponds to a zone of high interseismic coupling as measured by Global Positioning System (GPS) attributed to asperities in the downgoing plate (Chlieh *et al.*, 2014; Nocquet *et al.*, 2014). Immediately after the mainshock rupture, aseismic afterslip was observed and evolved over a 25-day period (Rolandone *et al.*, 2018). Two distinct patches of afterslip, each approximately 50 × 50 km, extended up-dip



**A Figure 2.** Earthquake epicenters and temporal sequence of events from automatic catalog produced from Incorporated Research Institutions for Seismology–Portable Array Seismic Studies of the Continental Lithosphere (IRIS-PASSCAL) stations, May 2016–May 2017, minimum of eight phases and errors less than 10 km, n = 2499 events. IRIS-PASSCAL stations blue triangles. Mainshock location and coseismic slip contours from Nocquet *et al.* (2017), coseismic slip contour 1 m, and maximum slip 6 m. Slab contours every 10 km depth from Slab2 (Hayes *et al.*, 2018). Temporal sequence of events plotted by latitude (vertical axis = latitude, horizontal axis = Julian day), circles scaled and color coded by magnitude: yellow  $M_L \ge 6$ , orange  $6 > M_L \ge 5$ , brown  $5 > M_L \ge 4$ , and red  $M_L < 4$ . Earthquake clusters designated by letters discussed in the Initial Observations section. See Figure 1 for topography and bathymetry scaling.

northwest and southwest of the mainshock rupture toward the trench. Cumulative afterslip and equivalent magnitude for the northern patch was up to 0.7 m and  $M_{\rm w}$  7.1; for the southern patch up to 1.0 m and  $M_{\rm w}$  7.0 (Rolandone *et al.*, 2018). The earthquake also triggered a SSE ~100 km south of the rupture with slip up to 0.8 m and equivalent moment magnitude of  $M_{\rm w}$  6.7–6.8 (Rolandone *et al.*, 2018). These same three regions experienced slow-slip earthquakes, earthquake swarms, and repeating earthquakes in the past (Holtkamp *et al.*, 2011; Vallee *et al.*, 2013; Segovia *et al.*, 2018; Vaca *et al.*, 2018). Within this initial 25-day period, an additional deep patch of aseismic afterslip was observed down-dip to the southeast of the mainshock rupture at 60 km depth (Rolandone *et al.*, 2018).

In the wake of the earthquake an international rapid response effort coordinated by the Instituto Geofisico at the Escuela Politécnica Nacional (IG-EPN) in Quito deployed accelerometers, seismometers, ocean-bottom seismometers (OBSs), and GPS receivers to record aftershocks and measure postseismic deformation (Font et al., 2016). In this article, we focus on the U.S. seismic portion of the rapid response effort using Incorporated Research Institutions for Seismology–Portable Array Seismic Studies of the Continental

Lithosphere (IRIS-PASSCAL) instruments (Meltzer and Beck, 2016). These data are openly available from the IRIS Data Management Center (DMC). We provide an overview of the data acquired, station locations, site conditions, data quality, and availability. We also discuss earthquake locations determined from these data over the 12-month temporary deployment and make available the earthquake catalog produced by automatic processing tools using the BRTT Antelope software (see Data and Resources). Finally, we use this and past experience to make recommendations to enhance rapid response deployments to better capture the unique observations that are only possible in the wake of large to great earthquakes.

#### THE PEDERNALES AFTERSHOCK DEPLOYMENT

Within three days of the 16 April 2016 Pedernales earthquake, a team from IG-EPN went to the epicentral region and deployed five broadband and five dual short-period strongmotion sensors. Between 9 and 22 May, teams from the United States (Lehigh University and University of Arizona), France (Université Côte d'Azur L'Institut de Recherche pour le Développement [IRD], Géoazur, and

Centre d'études et d'expertise sur les risques, l'environnement, la mobilité et l'aménagement [CEREMA]), and the United Kingdom (University of Liverpool) deployed a mix of short and intermediate period, and broadband sensors (Fig. 1). Short-period three-component OBSs were deployed by IRD at the end of May. The stations in the temporary aftershock deployment augment data recorded by the National Seismic Network (RENSIG; Alvarado *et al.*, 2018).

In total, 55 temporary stations were deployed on land over a 300 km  $\times$  90 km region (Fig. 1). An OBS deployed offshore near the trench extends lateral coverage to  $\sim$ 160 km and provides critical observations west of the mainshock and aftershock sequence. Station coverage adjacent to the 2016 rupture extends north to Esmeraldas in the vicinity of the 1958 rupture, and south to Manta where SSEs and earthquake swarms are common. The temporary deployment encompasses the aftershock zone of the previous 1942  $M_{\rm w}$  7.9 earthquake and the epicenter and part of the estimated rupture area of the 1906  $M_{\rm w}$  8.8 earthquake in Ecuador (Fig. 1).

On land, 35 broadband sensors, a mix of STS-2 (n = 9), CMG-3 (n = 10), and Trillium Compact sensors (n = 16) were deployed over the entire 300 × 90 km area covered by the temporary network (Fig. 1). Fourteen intermediate-period (CMG-40T) sensors were deployed in the central portion of the network adjacent to and south of the southern end of the rupture spanning a portion of the margin where lateral variation in plate coupling is observed (high to low, north to south; Chlieh et al., 2014). Six short-period (Lennartz LE 3D Lite) sensors were deployed in the southern portion of the network adjacent to where SSEs and earthquake swarms are observed. Station spacing within the network varied from 10 to 20 km. The distribution of sensors in part reflects coordination between the teams to limit the geographic area covered by each deployment team to speed up installation of the network (Ecuador [EC], north; United States [US], north; France [FR], central; and United Kingdom [UK], south). The 19 broadband stations from IRIS-PASSCAL were installed 11-16 May 2016 predominantly in the northern part of the network with a few stations deployed in the central and southern part of the network to infill broadband coverage (Figs. 1 and 2).

The majority of the stations in the temporary deployment remained in the field for 12 months. The OBSs recorded data for five and a half months and were removed in mid-November 2016. The 19 IRIS-PASSCAL stations were demobilized in early May 2017 along with most of the on land temporary stations. Twelve of the stations deployed by IRD remained in the field into August 2017.

All stations were deployed at low elevation sites in the fore-arc (Fig. 1). For the most part, the IRIS-PASSCAL stations are far from bedrock with sensors placed in soil varying from sandy, to organic rich, to almost solid clay (© Table S1, available in the supplemental content to this article). The one exception is EC19 where weathered ophiolite outcrops at the surface. By necessity, approximately one-third of the stations are along the coast. Much of Esmeraldas and Manabí provinces

are lightly populated, rural and agricultural with small-to-moderate-size towns and resort areas interspersed. The majority of the stations are in rural settings (© Fig. S1). For security, stations were located on the property of host families, generally (though not always) within proximity of houses (© Table S1). The IRIS-PASSCAL stations were recorded by RefTek RT130 data loggers at 100 samples per second. Each station was powered by a 12 V 100 amp hour deep cycle battery and a 65-watt solar panel. Sensor vaults were simple and easy to install quickly. Sensors were placed on granite tiles, covered with an inverted plastic barrel, and buried ~0.5–1.0 m below the surface (© Fig. S2).

#### DATA QUALITY AND AVAILABILITY

Data from the 19 IRIS-PASSCAL stations were archived at the IRIS DMC and openly available after service runs in September 2016 and March 2017 and after demobilization in May 2017. The average percent data recovery for the deployment was 92.4% with individual stations ranging from 50% to 100% (© Table S1 and Fig. S3). The only known sensor issue at the time of the initial deployment was at EC20 where the east component was bad.

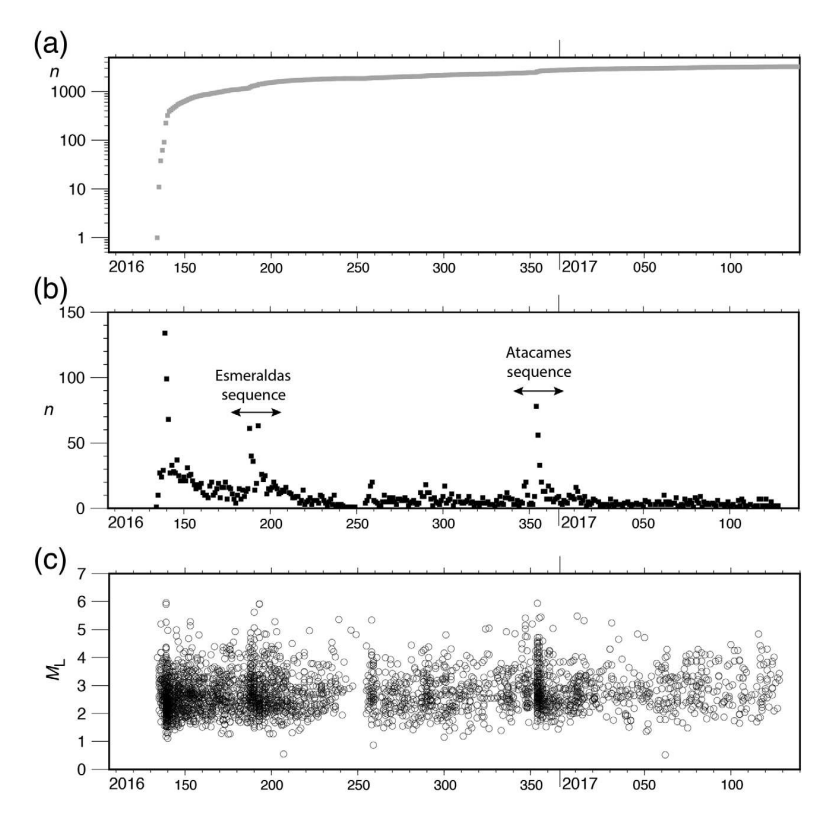
Over the course of the 12-month deployment, four additional sensors (EC01, EC04, EC06, and EC17/21) developed issues (© Table S1), two stations (EC11 and EC12) developed issues with the Ref Tek data-logger, and one station EC07 had data-logger and sensor cable issues. Over the course of the deployment, 8 of 19 stations (42%) had issues severe enough to impact data acquisition. The failure rate is in part due to environmental factors, high humidity in an equatorial environment (condensation), and significant rainfall during the rainy season, December through March (flooding of some vaults and station boxes), but it also reflects an aging broadband pool.

Representative frequency-dependent noise levels for stations in the temporary deployment are included in © Figure S4. For the most part, stations have intermediate noise levels in three period bands: 0.1–1, 1–10, and 10–100 s on the vertical component. Noise levels at long periods are higher on the horizontal components. Higher noise levels between 1 and 10 Hz reflect high earthquake activity associated with the aftershock sequence. There are no consistent differences in noise characteristics between coastal versus inland sites, soil versus bedrock sites, or between stations located tens versus hundreds of meters from local houses or buildings.

All data from the U.S. portion of the Pedernales earth-quake aftershock deployment are archived and openly available at the IRIS DMC, network code 8G (2016–2017) (see Data and Resources). Data from France and the United Kingdom, network code XE, will be available through Réseau Sismologique and Géodésique Français summer 2019.

# **AUTOMATIC EARTHQUAKE CATALOG**

Earthquake locations were determined for events recorded by the PASSCAL stations through automatic processing using tools



▲ Figure 3. (a) Cumulative number of events, (b) number of events per day, and (c) event magnitude per day from automatic catalog produced from IRIS-PASSCAL stations, May 2016–May 2017 minimum of eight phases and errors less than 10 km, n = 2499 events. Horizontal axis is Julian day. Partial data gap around jd250 due to disk storage problems. Uptick in seismicity associated with Esmeraldas and Atacames swarms labeled in (b).

from the BRTT Antelope software (see Data and Resources). Automatic detections were picked using short-term average (STA) versus long-term average (LTA) ratios on vertical and horizontal components for P and S waves, respectively (P waves: 1–10 Hz, STA/LTA > 4.0; S waves: 1–5 Hz, STA/LTA > 4.0). Detections are incorporated into potential earthquake arrivals using a precomputed travel-time grid built with the iasp91 velocity model. Hypocenter locations are determined via an iterative least-squares inversion of travel-time residuals (Pavlis *et al.*, 2004). Traditional Richter (local) magnitude ( $M_{\rm L}$ ) is calculated automatically for events with a minimum of three stations with a signal-to-noise ratio greater than 3.

The full catalog contains 3246 events. The magnitude of completeness  $M_c=2.3$  is estimated using the maximum curvature method (Wiemer and Katsumata, 1999; Wiemer and Wyss, 2000). Using  $M_c=2.3$  and the maximum-likelihood method for calculating b-values (Aki, 1965) and magnitude binning width of 0.1, results in b=0.88. Manual inspection of the automatic catalog indicates that events with at least eight phases and locations errors less than 10 km (using 68% confidence ellipses) are reliably earthquakes. Earthquakes were detected and associated with less than eight phases, but the

number of false detections or spurious signals is higher. Location errors and comparisons between the full catalog and events with at least eight phases are provided in © Figures S5 and S6. These formal uncertainties do not reflect any bias introduced using a 1D global velocity model in a region with 3D velocity heterogeneity. The full catalog, including magnitudes and uncertainties, is included in QuakeML format in the © supplemental content.

#### **INITIAL OBSERVATIONS**

Aftershocks of the Pedernales earthquake show a clear pattern of clustering within, around, and to the north and south of the rupture (Fig. 2). From south to north, earthquake clusters are observed under the coastline north of Manta (A in Fig. 2), up-dip and extending to the trench at the southern end of the rupture (B in Fig. 2), within the rupture zone between the two patches of higher slip (C in Fig. 2), up-dip at the trench and down-dip of the mainshock extending beneath the coast at the northern end of the rupture (D in Fig. 2), offshore Punta Galera 20 km north of the end of the rupture and on land east of the offshore Galera cluster (E in Fig. 2), ~70 km northeast of the mainshock in the vicinity of Atacames (F in Fig. 2), and ~100 km northeast of the mainshock at Esmeraldas (G in Fig. 2). The eastern downdip limit of seismicity is quite sharp (Fig. 2). The up-dip limit is more diffuse but this could change, as data from the OBS are included.

The cumulative number of events, number of events per day, and event magnitude per day indicate a high rate of seismicity that gradually decays with time (Fig. 3 and © animation in the supplemental content). Superimposed on this gradual decay are small bursts of activity, spatially focused higher rates of seismicity, lasting from several days up to a week. Higher magnitude events  $(5 \le M \le 7)$  are interspersed throughout the postseismic sequence up to 9 months after the mainshock. By the end of January 2017, both the magnitude and frequency of events decay to background levels through the end of the temporary deployment. Two significant upticks in seismicity correlate with an earthquake swarm in July 2016 at Esmeraldas and a series of moderate earthquakes  $(M_L 4-5)$ in December 2016 at Atacames. For the most part, both moderate-to-large and small-magnitude events occur within the clusters (Fig. 2). Notable exceptions are the cluster of events within the rupture zone between the two patches of larger slip (C in Fig. 2), and a cluster of events between the mainshock and the series of magnitude 6 earthquakes to the east (east end of D, Fig. 2). These two areas contain only smaller magnitude events (Fig. 2).

For the first two and a half months after the mainshock, earthquakes are generally restricted to Punta Galera and south (Fig. 2 and © animation in the supplemental content). On 18 June, a month after the mainshock, two large aftershocks,  $M_{\rm w}$  6.8 and 6.9 (USGS NEIC, 2017), occurred within 8 hr of each other, beneath the coast at the northern end of the rupture in an area where interseismic plate coupling is high (Nocquet et al., 2017; Rolandone et al, 2018). In July, an earthquake swarm occurred in the upper plate ~100 km northeast of the rupture beneath the town of Esmeraldas (Hoskins et al., 2018). The swarm occurred close to the southern edge of the 1958  $M_{\rm w}$  7.7 earthquake (Figs. 1 and 2). The swarm contains events with local magnitudes up to 5 within the sequence but is not preceded by a large-magnitude event. During the July swarm at Esmeraldas, two large earthquakes ( $M_{
m w}$  5.9 and 6.3, USGS NEIC, 2017) occurred in the earthquake cluster beneath the coast at the northern end of the rupture (Fig. 2). In contrast, the uptick in seismicity in December at Atacames begins with an  $M_{\rm w}$  5.2 event and contains multiple events of similar magnitude ( $M_w$  5.4, 4.8, and 4.8; USGS NEIC, 2017) over the next 7–9 days. Ground shaking associated with the 18 June events and the Esmeraldas and Atacames sequences caused additional damage to buildings weakened in the mainshock.

The general pattern of earthquake clustering from Punta Galera south was established within the first week of the mainshock (IG-EPN catalog; Rolandone et al., 2018). This clustering is also observed in the long-term catalog (from south to north the Manta, Jama, and Galera clusters; Font et al., 2013; Segovia et al., 2018; Vaca et al., 2018). These clusters outline regions of aseismic slip that evolved over a 25-day period after the mainshock (Rolandone et al., 2018), ending just as the temporary deployment was being installed. These regions continued to be the site of focused seismic activity for months and contain the majority of the magnitude 4 and larger events (Fig. 2). The Galera cluster lies between the northern end of the patch of aseismic slip and a region of high interseismic plate coupling associated with Punta Galera. The Jama cluster is associated with a region of high interseismic coupling (Collot et al., 2017; Nocquet et al., 2017; Rolandone et al., 2018).

North and northeast of the rupture, toward the epicentral regions of the 1906 and 1958 great earthquakes, the earthquake clusters with epicenters on land trending north toward Atacames align with the eastern boundary of Miocene Borbon basin (Reyes and Michaud, 2012) and a break in topography associated with uplifted Miocene sediments. A series of crustal faults (e.g., Galera fault, Mache lineament, and others) are mapped in this area and farther east toward Esmeraldas (Eguez et al., 2003). The relationship between observed seismicity and crustal faults is being explored using high-precision earthquake relocation methods.

Earthquake catalogs combining data from the complete rapid response deployment (EC, US, FR, and UK temporary stations) and permanent network stations have been completed (Agurto-Detzel *et al*, 2018). These catalogs support the

observations presented here but reveal additional detail on the temporal and spatial evolution of the sequence of events following the Pedernales earthquake, especially in the central and southern portions of the temporary deployment. The number of events detected using stations from the complete temporary array increased threefold, and the magnitude of completeness improved by 0.5 to  $M_{\rm c}=1.8$ . Preliminary joint inversion for earthquake location and 3D velocity structure shifts event locations within individual earthquake clusters but does not shift the spatial distribution of the clusters themselves.

### **LESSONS LEARNED**

Although the seismic rapid response deployment after the Pedernales earthquake was relatively smooth and efficient, improvements in instrumentation and protocols established in advance of destructive events are needed to facilitate rapid deployments and field studies after large subduction-zone earthquakes. Rapid response deployments have the potential to uniquely capture a range of subduction-zone processes complementing the observations from permanent networks to shed new light on rupture of megathrust earthquakes and transient processes associated with these events. Real-time data from rapid response deployments can be used to monitor the postseismic evolution of aftershock sequences and triggered seismicity to improve aftershock forecasting and seismic hazard assessment immediately after large-magnitude events. Systemic changes are needed in rapid response deployments to maximize what we can learn about earthquake rupture and postseismic response, and to reduce risk in the wake of large-magnitude earthquakes.

After a large earthquake, time is of the essence to capture the immediate postseismic response. The first stations from the international rapid response effort were installed three weeks after the mainshock. This reflects the time required to marshal resources (financial, technical, and human), ship instruments, arrange customs clearance, acquire materials and supplies, and arrange transportation to the field. This time needs to be shortened to no more than 48-72 hrs. Advance planning and regional instrument pools can ensure that protocols are in place and resources accessible to speed the time between event and response. Appropriate robust instrumentation is needed, which can be deployed easily and quickly and operate reliably in a range of environments and site conditions. Integrated systems are needed that take advantage of new options for power supply, allow for multiple collocated sensors to record the full spectrum of ground motions (strong to weak), include options for real-time communications, and directly capture and log metadata. Rapid response efforts need to adopt a system approach from instrument deployment to data capture and integration, time-series analysis, and data products including robust earthquake locations, magnitudes, and source characterization. Coordination, collaboration, and near-real-time open data should be the standard for all rapid response efforts.

## **DATA AND RESOURCES**

All data from the U.S. portion of the Pedernales earth-quake aftershock deployment can be obtained from the Incorporated Research Institutions for Seismology (IRIS) Data Management Center available at <a href="http://www.iris.edu/dms/nodes/dmc/">http://www.iris.edu/dms/nodes/dmc/</a> (last accessed November 2018), network code 8G (2016–2017), doi: 10.7914/SN/8G\_2016. The full automatic catalog is included in the © supplemental content to this article in QuakeML format. Maps and figures were made using the Generic Mapping Tools v.5.2.1 available at <a href="http://gmt.soest.hawaii.edu">http://gmt.soest.hawaii.edu</a> (last accessed November 2018) (Wessel *et al.*, 2013). The other information about BRTT Antelope software can be found at <a href="http://www.brtt.com">http://www.brtt.com</a> (last accessed June 2018). Instituto Geofísico at the Escuela Politécnica Nacional (IG-EPN) catalog can be accessed at <a href="https://www.igepn.edu.ec">https://www.igepn.edu.ec</a> (last accessed September 2017).

## **ACKNOWLEDGMENTS**

The U.S. Seismic Rapid Response deployment was supported by the National Science Foundation (NSF) Rapid Response Research (RAPID) Program Award Number EAR-1642498 and by the Portable Array Seismic Studies of the Continental Lithosphere (PASSCAL) facility of the Incorporated Research Institutions for Seismology (IRIS) through the PASSCAL Instrument Center at New Mexico Tech with support from the NSF under Cooperative Agreement Number EAR-1261681 and by the Department of Energy National Nuclear Security Administration. Financial support for the international rapid response effort was provided by: the Instituto Geofísico at the Escuela Politécnica Nacional (IG-EPN) in Quito Ecuador; L'Institut de Recherche pour le Développement (IRD) Géoazur at Université de la Côte d'Azur, and Centre d'études et d'expertise sur les risques, l'environnement, la mobilité et l'aménagement (CEREMA) France; and the Natural Environment Research Council (NERC) in the United Kingdom. The authors thank the U.S. Embassy in Quito for expediting customs clearance for the IRIS-PASSCAL instrument shipment. The authors are grateful to Emilio Acosta, Carlos Ayol, Christian Cisneros, Marcos Cordova, Pablo Cruz, Carlos Macias, Marcelo Ortiz, Daniel Pacheco, Xavier Parra, Gabriela Ponce, Mónica Segovia, Daniel Sierra, Juan Carlos Singaucho, Ivan Tapa, Roberto Toapanda, and Mayra Vaca from IG-EPN for their assistance with logistics and fieldwork. They are also grateful to the many people of Esmeraldas and Manabí provinces, who allowed us to install stations on their property and made sure the stations were secure during the deployment. The authors thank the anonymous reviewers for helpful comments to improve the article.

#### **REFERENCES**

Agurto-Detzel, H., Y. Font, P. Charvis, A. P. Alvarado, D. Ambrois, S. L. Beck, M. Hoskins, S. L. Rios, C. Lynner, A. Meltzer, et al. (2018). Aftershocks of the 2016  $M_{\rm w}$  7.8 Ecuador Earthquake Reveal

- Earthquake Cycle is Controlled by Long-Lived Structures, T52B-04, 2018 AGU Fall Meeting, AGU, Washington D.C., 10–14 December
- Aki, K. (1965). Maximum likelihood estimate of b in the formula  $\log N = a bM$  and its confidence limits, *Bull. Earthq. Res. Inst.* **43**, 237–239.
- Alvarado, A., M. Ruiz, P. Mothes, H. Yepes, M. Segovia, M. Vaca, C. Ramos, W. Enríquez, G. Ponce, P. Jarrín, et al. (2018). Seismic, volcanic, and geodetic networks in Ecuador: Building capacity for monitoring and research, Seismol. Res. Lett. 89, no. 2A, doi: 10.1785/0220170229.
- Bangs, N. L. B., S. P. S. Gulick, and T. H. Shipley (2006). Seamount subduction erosion in the Nankai trough and its potential impact on the seismogenic zone, *Geology* 34, no. 8, 701–704.
- Beck, S. L., and L. J. Ruff (1984). The rupture process of the Great 1979 Colombia earthquake: Evidence for the asperity model, *J. Geophys. Res.* 89, no. 11, 9281–9291.
- Bilek, S. L., and T. Lay (2018). Subduction zone megathrust earthquakes, Geosphere 14, no. 4, 1468–1500, doi: 10.1130/GES01608.1.
- Brodsky, E. E., and T. Lay (2014). Geophysics. Recognizing foreshocks from the 1 April 2014 Chile earthquake, *Science* **344**, no. 6185, 700–702, doi: 10.1126/science.1255202.
- Brown, J. R., G. C. Beroza, S. Ide, K. Ohta, D. R. Shelly, S. Y. Schwartz, W. Rabbel, M. Thorwart, and H. Kao (2009). Deep low-frequency earthquakes in tremor localize to the plate interface in multiple subduction zones, *Geophys. Res. Lett.* 36, no. 19, doi: 10.1029/ 2009GL040027.
- Brown, J. R., S. G. Prejean, G. C. Beroza, J. S. Gomberg, and P. J. Haeussler (2013). Deep low-frequency earthquakes in tectonic tremor along the Alaska-Aleutian subduction zone, *J. Geophys. Res.* **118**, no. 3, 1079–1090, doi: 10.1029/2012/B009459.
- Chlieh, M., P. A. Mothes, J. M. Nocquet, P. Jarrin, P. Charvis, D. Cisneros, Y. Font, J. Y. Collot, J. C. Villegas-Lanza, F. Rolandone, et al. (2014). Distribution of discrete seismic asperities and ascismic slip along the Ecuadorian megathrust, Earth Planet. Sci. Lett. 400, 292–301, doi: 10.1016/j.epsl.2014.05.027.
- Collot, J.-Y., B. Marcaillou, F. Sage, F. Michaud, W. Agudelo, P. Charvis, D. Graindorge, M.-A. Gutscher, and G. Spence (2004). Are rupture zone limits of great subduction earthquakes controlled by upper plate structures? Evidence from multichannel seismic reflection data acquired across the northern Ecuador–southwest Colombia margin, J. Geophys. Res. 109, no. B11103, doi: 10.1029/2004JB003060.
- Collot, J.-Y., É. Sanclemente, J. M. Nocquet, A. Leprêtre, A. Ribodetti, P. Jarrin, M. Chlieh, D. Graindorge, and P. Charvis (2017). Subducted oceanic relief locks the shallow megathrust in central Ecuador, J. Geophys. Res. 122, no. 5, 3286–3305, doi: 10.1002/2016[B013849.
- Dragert, G., K. Wang, and T. S. James (2001). A silent slip event on the deeper Cascadia subduction interface, *Science* **292**, no. 5521, 1525–1528, doi: 10.1126/science.1060152.
- Eguez, A., A. Alvarado, H. Yepes, M. Machette, C. Costa, and R. Dart (2003). Database and map of Quaternary faults and folds of Ecuador and its offshore regions, *U.S. Geol. Surv. Open-File Rept. 03-289*, 71 pp.
- Font, Y., M. C. Ruiz, A. P. Alvarado, D. Mercerat, S. L. Beck, S. Leon Rios, A. Meltzer, P. Charvis, M. M. Regnier, P. Jarrin, et al. (2016). International postseismic response after the  $M_{\rm w}=7.8$  April 16, 2016 Pedernales earthquake in Ecuador, American Geophysical Union, Fall Meeting 2016, Abstract T51E–2977.
- Font, Y., M. Segovia, S. Vaca, and T. Theunissen (2013). Constraints from earthquake location in a 3-D a priori velocity model, *Geophys. J. Int.* **193**, no. 1, doi: 10.1093/gji/ggs083.
- Franco, G., H. Stone, B. Ahmed, S. C. Chian, F. Hughes, N. Jirouskova, S. Kaminski, J. Lopez, N. van Drunen, and M. Querembas (2017). The April 16 2016  $M_{\rm w}$  7.8 Muisne earthquake in Ecuador—Preliminary observation from the EEFIT reconnaissance mission of May 24–June 7, 16th World Conf. on Earthquake Engineering, Santiago, Chile, 8–13 January 2017, 1–12.

- Goretti, A., C. Molina, and L. Hedelund (2017). Post-earthquake safety evaluation of buildings in Portoviejo, Manabí province, following the  $M_{\rm w}$  7. 8 Ecuador earthquake of April 16, 2016, *Int. J. Disast. Risk Reduct.* 24, 271–283, doi: 10.1016/j.ijdrr.2017.06.011.
- Hayes, G. P., G. L. Moore, D. E. Portner, M. Hearne, H. Flamme, M. Furtney, and G. M. Smoczyk (2018). Slab2, a comprehensive subduction zone geometry model, *Science* 362, no. 6410, doi: 10.1126/science.aat4723.
- Hicks, S. P., A. Rietbrock, I. M. A. Ryder, C. S. Lee, and M. Miller (2014). Anatomy of a megathrust: The 2010 M 8.8 Maule, Chile earth-quake rupture zone imaged using seismic tomography, Earth Planet. Sci. Lett. 405, 142–155, doi: 10.1016/j.epsl.2014.08.028.
- Holtkamp, S. G., M. E. Pritchard, and R. B. Lohman (2011). Earthquake swarms in South America, *Geophys. J. Int.* 187, no. 1, 128–146, doi: 10.1111/j.1365-246X.2011.05137.x.
- Hoskins, M., A. Meltzer, L. Soto-Cordero, J. Stachnik, S. L Beck, C. Lynner, M. Calixto Ruiz, A. Patricia Alvarado, S. Hernandez, P. Charvis, et al. (2018). Variable slip modes in postseismic deformation north of the April 16, 2016 M<sub>w</sub> 7.8 Pedernales, Ecuador megathrust earthquake, American Geophysical Union, Fall Meeting 2018, Washington D.C., 10–14 December, Abstract T43E–0444.
- Husen, S., and E. Kissling (2002). Tomographic evidence for a subducted seamount beneath the Gulf of Nicoya, Costa Rica: The cause of the 1990  $M_{\rm w}=7.0$  Gulf of Nicoya earthquake, *Geophys. Res. Lett.* **29**, no. 8, 1990–1993.
- Ide, S. (2012). Variety and spatial heterogeneity of tectonic tremor world-wide, J. Geophys. Res. 117, no. B3, doi: 10.1029/2011JB008840.
- International Federation of Red Cross and Red Crescent Societies (2016). Revised Appeal MDREC012, available at http://www.ifrc.org/en/publications-and-reports/appeals/?p=2 (last accessed November 2016).
- Kanamori, H. (2014). The diversity of large earthquakes and its implications for hazard mitigation, Ann. Rev. Earth Planet. Sci. 42, no. 1, 7–26, doi: 10.1146/annurev-earth-060313-055034.
- Kanamori, H., and K. C. McNally (1982). Variable rupture mode of the subduction zone along the Ecuador–Colombia coast, *Bull. Seismol.* Soc. Am. 72, no. 4, 1241–1253.
- Kelleher, J. A. (1972). Rupture zones of large South American earth-quakes and some predictions, J. Geophys. Res. 77, no. 11, 2087–2103, doi: 10.1029/JB077i011p02087.
- Kodaira, S. (2000). Subducted seamount imaged in the rupture zone of the 1946 Nankaido earthquake, Science 289, no. 5476, 104–106.
- Lanning, F., A. G. Haro, M. K. Liu, A. Monzon, H. Monzon-Despang, A. Schultz, and A. Tola (2016). EERI Earthquake Reconnaissance Team Report, 92 pp., ISBN: 978-1-932884-69-2, available at http://learningfromearthquakes.org/2016-04-16-muisne-ecuador/images/2016\_04\_16\_Muisne\_Ecuador/pdfs/EERI-Ecuador-2016-Recon-Report-Reduced.pdf (last accessed October 2018).
- Lowry, A. R., K. M. Larson, V. Kostoglodov, and R. Bilham (2001). Transient fault slip in Guerrero, Southern Mexico, Geophys. Res. Lett. 28, no. 19, 3753–3756.
- Mayorga, E. F., and J. J. Sánchez (2016). Modelling of Coulomb stress changes during the great (M<sub>w</sub> = 8.8) 1906 Colombia–Ecuador earthquake, J. South Am. Earth Sci. 70, 268–278, doi: 10.1016/ j.jsames.2016.05.009.
- Meltzer, A., and S. Beck (2016). 2016 Pedernales Earthquake Aftershock
  Deployment Ecuador, International Federation of Digital
  Seismograph Networks, Other/Seismic Network, doi: 10.7914/
  SN/8G 2016
- Mendoza, C., and J. W. Dewey (1984). Seismicity associated with the great Colombia–Ecuador earthquakes of 1942, 1958 and 1979: Implications for barrier models of earthquake rupture, *Bull. Seismol. Soc. Am.* 74, no. 2, 577–593.
- Nocquet, J.-M., P. Jarrin, M. Vallée, P. A. Mothes, R. Grandin, F. Rolandone, B. Delouis, H. Yepes, Y. Font, D. Fuentes, et al. (2017). Supercycle at the Ecuadorian subduction zone revealed after the 2016 Pedernales earthquake, Nature Geosci. 10, no. 2, 145–149, doi: 10.1038/ngeo2864.

- Nocquet, J.-M., J. C. Villegas-Lanza, M. Chlieh, P. A. Mothes, F. Rolandone, P. Jarrin, D. Cisneros, A. Alvarado, L. Audin, F. Bondoux, et al. (2014). Addendum: Motion of continental slivers and creeping subduction in the northern Andes, Nature Geosci. 7, no. 8, 612, doi: 10.1038/ngeo2217.
- Obara, K. (2002). Nonvolcanic deep tremor associated with subduction in southwest Japan, *Science* **296**, no. 5573, 1679–1681, doi: 10.1126/science.1070378.
- Palacios, P., H. Yepes, J. Marrero, and P. Ramón (2018). Site effects characterization at Portoviejo City (Ecuador) by normalizing seismic noise spectra using aftershocks, doi: 10.13140/RG.2.2.22681.93285.
- Pavlis, G. L., F. Vernon, D. Harvey, and D. Quinlan (2004). The generalized earthquake-location (GENLOC) package: An earthquake-location library, *Comput. Geosci.* 30, nos. 9/10, 1079–1091, doi: 10.1016/j.cageo.2004.06.010.
- Peng, Z., and J. Gomberg (2010). An integrated perspective of the continuum between earthquakes and slow-slip phenomena, *Nature Geosci.* 3, 599–607, doi: 10.1038/NGEO940.
- Peterson, C. L., and D. H. Christensen (2009). Possible relationship between nonvolcanic tremor and the 1998–2001 slow slip event, south central Alaska, J. Geophys. Res. 114, no. B6, doi: 10.1029/ 2008IB006096.
- Reyes, P., and F. Michaud (2012). *Mapa Geológico de la Margen Costera Ecuatoriana (1:50000)*, EP PetroEcuador, Quito, Ecuador (in Spanish).
- Rogers, G., and H. Dragert (2003). Episodic tremor and slip on the Cascadia subduction zone: The chatter of silent slip, *Science* 300, no. 5627, 1942–1943, doi: 10.1126/science.1084783.
- Rolandone, F., J. M. Nocquet, P. A. Mothes, P. Jarrin, M. Vallée, N. Cubas, S. Hernandez, M. Plain, S. Vaca, and Y. Font (2018). Areas prone to slow slip events impede earthquake rupture propagation and promote afterslip, *Sci. Adv.* 4, no. 1, 2–10, doi: 10.1126/sciadv.aao6596.
- Saffer, D. M., and L. M. Wallace (2015). The frictional, hydrologic, metamorphic and thermal habitat of shallow slow earthquakes, *Nature Geosci.* 8, no. 8, 594–600, doi: 10.1038/ngeo2490.
- Schwartz, S. Y., and J. M. Rokosky (2007). Slow slip events and seismic tremor at circum-pacific subduction zones, *Rev. Geophys.* 45, no. 3, doi: 10.1029/2006RG000208.
- Segovia, M., Y. Font, M. Régnier, P. Charvis, A. Galve, J. M. Nocquet, P. Jarrín, Y. Hello, M. Ruiz, and A. Pazmiño (2018). Seismicity distribution near a subducting seamount in the central Ecuadorian subduction zone, space–time relation to a slow-slip event, Tectonics 37, no. 7, 2106–2123, doi: 10.1029/2017TC004771.
- Shelly, D. R., G. C. Beroza, and S. Ide (2007). Complex evolution of transient slip derived from precise tremor locations in western Shikoku, Japan, Geochem. Geophys. Geosyst. 8, no. 10, doi: 10.1029/2007GC001640.
- Sherrod, B., and J. Gomberg (2014). Crustal earthquake triggering by prehistoric great earthquakes on subduction zone thrusts, *J. Geophys. Res.* 119, no. 2, 1273–1294.
- Swenson, J. L., and S. L. Beck (1996). Historical 1942 Ecuador and 1942 Peru subduction earthquakes, and earthquake cycles along Colombia–Ecuador and Peru subduction segments, *Pure Appl. Geophys.* 146, no. 1, 67–101, doi: 10.1007/BF00876670.
- U.S. Geological Survey National Earthquake Information Center (USGS NEIC) (2016). M 7.8 27km SSE of Muisne, Ecuador USGS Earthquake Hazards Program, available at https://earthquake.usgs.gov/earthquakes/eventpage/us20005j32/executive (last accessed June 2017).
- USGS NEIC (2017). Search Earthquake Catalog—USGS Earthquake Hazards Program, retrieved from https://earthquake.usgs.gov/earthquakes/search/ (last accessed June 2017).
- Vaca, S., M. Vallée, J. M. Nocquet, J. Battaglia, and M. Régnier (2018). Recurrent slow slip events as a barrier to the northward rupture propagation of the 2016 Pedernales earthquake (central Ecuador), *Tectonophysics* 724/725, 80–92, doi: 10.1016/j.tecto.2017.12.012.

Vallee, M., J. M. Nocquet, J. Battaglia, Y. Font, M. Segovia, M. Regnier, P. Mothes, P. Jarrin, D. Cisneros, S. Vaca, et al. (2013). Intense interface seismicity triggered by a shallow slow slip event in the central Ecuador subduction zone, J. Geophys. Res. 118, no. 6, 2965–2981, doi: 10.1002/jgrb.50216.

Wallace, L. M., and D. Eberhart-Phillips (2013). Newly observed, deep slow slip events at the central Hikurangi margin, New Zealand: Implications for downdip variability of slow slip and tremor, and relationship to seismic structure, *Geophys. Res. Lett.* 40, no. 20, 5393–5398, doi: 10.1002/2013GL057682.

Wang, K., and S. L. Bilek (2011). Do subducting seamounts generate or stop large earthquakes? *Geology* **39**, no. 9, 819–822.

Wang, K., and S. L. Bilek (2014). Invited review paper: Fault creep caused by subduction of rough seafloor relief, *Tectonophysics* **610**, 1–24.

Wessel, P., W. H. F. Smith, R. Scharroo, J. Luis, and F. Wobbe (2013). Generic mapping tools: Improved version released, *Eos Trans. AGU* 94, no. 45, 409–410, doi: 10.1002/2013EO450001.

Wiemer, S., and K. Katsumata (1999). Spatial variability of seismicity parameters in aftershocks zones, J. Geophys. Res. 104, no. B6, 13,135–13,151.

Wiemer, S., and M. Wyss (2000). Minimum magnitude of completeness in earthquake catalogs: Examples from Alaska, the western United States, and Japan, *Bull. Seismol. Soc. Am.* **90**, no. 4, 859–869, doi: 10.1785/0119990114.

Ye, L., H. Kanamori, J.-P. Avouac, L. Li, K. F. Cheung, and T. Lay (2016). The 16 April 2016,  $M_{\rm W}$  7.8 ( $M_{\rm S}$  7.5) Ecuador earthquake: A quasi-repeat of the 1942  $M_{\rm S}$  7.5 earthquake and partial re-rupture of the 1906  $M_{\rm S}$  8.6 Colombia–Ecuador earthquake, Earth Planet. Sci. Lett. 454, 248–258, doi: 10.1016/j.epsl.2016.09.006.

Anne Meltzer
Mariah Hoskins
Lillian Soto-Cordero
Joshua C. Stachnik
Department of Earth and Environmental Sciences
Lehigh University
1 West Packer Avenue
Bethlehem, Pennsylvania 18015 U.S.A.
ameltzer@lehigh.edu
mac716@lehigh.edu
lis213@lehigh.edu
jcstachnik@gmail.com

Susan Beck
Colton Lynner
Rob Porritt'
Daniel Portner
Department of Geosciences
University of Arizona
1040 East 4th Street
Tucson, Arizona 85721 U.S.A.
slbeck@email.arizona.edu
colton.lynner@gmail.com
rporritt@ig.utexas.edu
portner@email.arizona.edu

Mario Ruiz
Alexandra Alvarado
Stephen Hernandez
Hugo Yepes
Instituto Geofísico at the Escuela Politécnica Nacional
Ladrón de Guevara E11-253
Apartado 2759, Quito, Ecuador
mruiz@igepn.edu.ec
aalvarado@igepn.edu.ec
hernandez.stephen@gmail.com
hyepes@igepn.edu.ec

Philippe Charvis
Yvonne Font
Marc Regnier
Hans Agurto-Detzel
Université Côte d'Azur IRD
Géoazur
250 rue Albert Einstein
Sophia Antipolis
06560 Valbonne, France
philippe.charvis@geoazur.unice.fr
regnier@geoazur.unice.fr
agurto@geoazur.unice.fr

Andreas Rietbrock<sup>2</sup>
Sergio Leon-Rios<sup>2</sup>
Department of Earth, Ocean and Ecological Sciences
University of Liverpool
Jane Herdman Building, 4 Brownlow Street
Liverpool L69 3GP, United Kingdom
andreas.rietbrock@kit.edu
sergio.leon-rios@kit.edu

E. Diego Mercerat CEREMA Méditerranée Project Team MOUVGS Géoazur 250 rue Albert Einstein Sophia Antipolis 06560 Valbonne, France diego.mercerat@cerema.fr

Published Online 6 March 2019

 $<sup>^1</sup>$  Now at the Institute for Geophysics, University of Texas, 10100 Burnet Road, Austin, Texas 78758 U.S.A.

<sup>&</sup>lt;sup>2</sup> Now at Geophysical Institute (GPI), Karlsruhe Institute of Technology, Hertzstrase 16, 76187 Karlsruhe, Germany.